COMPUTER METHODS AND PROGRAMS IN BIOMEDICINE 122 (2015) 76–88

journal homepage: www.intl.elsevierhealth.com/journals/cmpb

Investigation of factors affecting hypothermic pelvic tissue cooling using bio-heat simulation based on MRI-segmented anatomic models

Yuting Lin[a], *Wei-Ching Lin*[b], *Peter T. Fwu*[a], *Tzu-Ching Shih*[c], *Lee-Ren Yeh*[d], *Min-Ying Su*[a], *Jeon-Hor Chen*[a,d,*]

[a] *Tu and Yuen Center for Functional Onco-Imaging of Department of Radiological Sciences, University of California, Irvine, CA 92697, USA*

[b] *Department of Radiology, China Medical University Hospital, Taichung 40402, Taiwan*

[c] *Department of Biomedical Imaging and Radiological Science, China Medical University, Taichung 40402, Taiwan*

[d] *Department of Radiology, E-Da Hospital and I-Shou University, Kaohsiung 82445, Taiwan*

ARTICLE INFO

Article history:
Received 13 March 2015
Received in revised form 8 June 2015
Accepted 3 July 2015

Keywords:
Endorectal cooling balloon
Magnetic resonance imaging
Prostate
Neurovascular bundle

ABSTRACT

This study applied a simulation method to map the temperature distribution based on magnetic resonance imaging (MRI) of individual patients, and investigated the influence of different pelvic tissue types as well as the choice of thermal property parameters on the efficiency of endorectal cooling balloon (ECB). MR images of four subjects with different prostate sizes and pelvic tissue compositions, including fatty tissue and venous plexus, were analyzed. The MR images acquired using endorectal coil provided a realistic geometry of deformed prostate that resembled the anatomy in the presence of ECB. A single slice with the largest two-dimensional (2D) cross-sectional area of the prostate gland was selected for analysis. The rectal wall, prostate gland, peri-rectal fatty tissue, peri-prostatic fatty tissue, peri-prostatic venous plexus, and urinary bladder were manually segmented. Pennes' bio-heat thermal model was used to simulate the temperature distribution dynamics, by using an in-house finite element mesh based solver written in MATLAB. The results showed that prostate size and periprostatic venous plexus were two major factors affecting ECB cooling efficiency. For cases with negligible amount of venous plexus and small prostate, the average temperature in the prostate and neurovascular bundles could be cooled down to 25 °C within 30 min. For cases with abundant venous plexus and large prostate, the temperature could not reach 25 °C at the end of 3 h cooling. Large prostate made the cooling difficult to propagate through. The impact of fatty tissue on cooling effect was small. The filling of bladder with warm urine during the ECB cooling procedure did not affect the temperature in the prostate or NVB. In addition to the 2D simulation, in one case a 3D pelvic model

Abbreviations: MRI, magnetic resonance imaging; ECB, endorectal cooling balloon; 2D, two-dimensional; NVB, neurovascular bundle; PSA, prostate specific antigen; NFS-T2WI, non-fat-saturated T2 weighted images; FS-T2WI, fat-saturated T2 weighted images; FSE, fast spin echo; FOV, field of view; TR, repetition time; TE, echo time; P, prostate gland; RW, rectal wall; RF, peri-rectal fatty tissue; PF, peri-prostatic fatty tissue; PV, peri-prostatic venous plexus; B, urinary bladder; ROI, region of interest; FEM, finite element model; HIFU, high-intensity focused ultrasound; 3D, three-dimensional; IV, intravenous; LIIT, laser induced interstitial thermotherapy.

* *Corresponding author at*: No. 164, Irvine Hall, Tu and Yuen Center for Functional Onco-Imaging of Radiological Sciences, University of California, Irvine, CA 92697, USA. Tel.: +1 949 824 9327; fax: +1 949 824 3481.

E-mail address: jeonhc@uci.edu (J.-H. Chen).

http://dx.doi.org/10.1016/j.cmpb.2015.07.002

was constructed for volumetric simulation. It was found that the 2D slice with the largest cross-sectional area of prostate had the most abundant venous plexus, and was the most difficult slice to cool, thus it may provide a conservative prediction of the cooling effect. This feasibility study demonstrated that the simulation tool could potentially be used for adjusting the setting of ECB for individual patients during hypothermic radical prostatectomy. Further studies using MR thermometry are required to validate the in silico results obtained using simulation.

1. Introduction

The impact of radical prostatectomy on the quality of life, including the complications on the continence and sexual function, is the main concern for patients electing to receive surgery [1,2]. In patients receiving radical prostatectomy, the dissection of the bladder neck, mobilization of the neurovascular bundles (NVBs), and transection of the urethra–external sphincter complex, cause primary acute traumatic injury. The tissue damage is associated with the direct mechanical trauma of dissection, traction, as well as thermal energy that leads to neurapraxia or axonotmesis of pelvic autonomic nerves and muscle degeneration [3,4]. The tissue inflammation may lead to the secondary wave of damage. Radical prostatectomy undoubtedly causes direct trauma and inflammatory damage to surrounding neuromuscular tissues (i.e., bladder, urethra, and nerves) that may contribute to urinary incontinence and sexual dysfunction. The inflammatory cascade includes neutrophil and macrophage infiltration with subsequent release of proteolytic enzymes, activation of coagulation factors, proinflammatory cytokine formation, hypoxia, acidosis, free radical production, and apoptosis [5,6]. It has been shown that the use of local hypothermia during robot-assisted laparoscopic prostatectomy can attenuate this injury [7–10]. Preemptive hypothermia protects tissues from damage by lowering their metabolic rates and oxygen demands [11–16]. For each degree the temperature is decreased, a 5% reduction in oxygen consumption is achieved [11], which results in less lactate formation, preserved protein synthesis and cell signaling, and decreased inflammatory response [12].

It has also been established that cooling using endorectal cooling balloon (ECB) can significantly reduce the recovery time to regain urinary continence and sexual function in men [1,2,4,17], presumably due to the profound effects in reducing an array of tissue damage coming from the direct trauma and the inflammatory reaction [11]. The ECB was fabricated using a 5″ × 2.5″ elliptical balloon fused to a 40 cm, 24-french, three-way latex urethral catheter. The balloon, which was cycled continuously with 4 °C saline, was inserted through anus and conformed to the rectal wall [18]. Previous studies have shown that among men 65 years or older, there was a significant shortening of time in regaining continence and sexual function with lower temperatures [18–23], thus the use of ECB may lead to a better surgical outcome with improved quality of life.

Currently, the ECB procedure is done for all patients in a standard fashion. Anatomically, the ECB is designed to extend from the membranous urethra to the seminal vesicles. All patients are cooled using the same set-up, and there is no consideration for the different anatomy of individual patients to ensure effective cooling of the NVBs and the prostate gland [18,19]. For example, the size of the prostate, the amount of fat, and the presence of blood vessels in the pelvic regions may affect the cooling results significantly. An individualized temperature distribution map for each patient can be obtained using a thermal simulation model, by using the bioheat transfer equation based on the anatomical distribution of different tissues and their respective thermal properties in the pelvic region. The purposes of this exploratory simulation study are: (1) to investigate the effectiveness of ECB cooling by estimating the temperature that can be reached in NVB and the whole prostate in patients with different pelvic anatomies and tissue characteristics; (2) to evaluate how different tissue components will impact the effectiveness of ECB cooling. In particular, the amount of blood vessels, such as the periprostatic venous plexus, may be very different from patient to patient, and this "heat sink" effect will diminish the cooling effect, which can be investigated by comparing patients with and without extensive peri-prostatic venous plexus. The size of the prostate also varies among patients, and thus a patient with a large prostate may not be cooled efficiently. To investigate this effect, patients with large and small prostates are compared. In addition, the influence of the fat volume and the filling of bladder are considered.

In this work the simulation was focused on a 2-dimensional (2D) transverse slice that had the largest cross-sectional area of the prostate. At the base of the prostate the venous plexus was the most abundant, thus representing the worse scenario in cooling; also the NVB was very close to the prostate at this location, and most likely to be damaged by the surgical procedure. Therefore, the simulation done on this 2D slice can provide important clinically relevant information. In one case, we also constructed a 3-dimensional (3D) model for simulation, and the obtained results were compared to those of the 2D model. Similar to the concept of developing individualized treatment planning tool for radiation therapy, the ultimate goal of this project is to develop a patient-specific hypothermia surgical planning tool.

2. Materials and methods

2.1. *Subjects and image acquisition*

Four subjects with different pelvic tissue anatomy, including fatty tissue abundance, periprostatic venous abundance and prostate size were analyzed in this study. These subjects were clinically suspected to have prostate cancer due to elevated

prostate specific antigen (PSA) levels [24] and received prostate MR imaging for diagnostic purposes. The MRI study was performed on a GE Signa-HDx 3T MR scanner (GE Healthcare, Milwaukee, WI) using an endorectal coil. The images acquired using the endorectal coil could provide a realistic geometry of deformed prostate that resembled the anatomy in the presence of endorectal cooling balloon.

For each patient, two sets of images were used for tissue segmentation, non-fat-saturated T2 weighted images (NFS-T2WI) and fat-saturated T2 weighted images (FS-T2WI) [25], both acquired using the fast spin echo (FSE) sequences. The imaging parameters for NFS-T2WI were repetition time (TR)/echo time (TE) = [3950–5250]/[99–101] ms, echo train length = [16–21], slice thickness = 4 mm, matrix = 256 × 224 or 288 × 192 and field of view (FOV) = 180–200 mm. The imaging parameters for FS-T2WI were TR/TE = 5716/[103–109] ms, echo train length = 21, slice thickness = 4 mm, matrix = 288 × 192 and FOV = 180–200 mm. The images were acquired in axial (transverse) sections starting from above bilateral hip joints level down to symphysis pubis level. Regardless of the pelvic size of the subjects, a total of 22 slices were acquired for all patients. The range of 8.8 cm was more than sufficient to cover the superior-inferior direction of the prostate and surrounding tissues. The pixel depth for the MR image was 16 bits. The segmented images were saved as 8 bits mask files.

2.2. *Image segmentation*

In this feasibility study, a 2D simulation was performed to simplify the segmentation procedure and reduce computational burden. Based on the size of the segmented prostate on each acquired transverse slice, the slice that showed the largest 2D cross-sectional area of the prostate gland was chosen for the analysis. Besides the prostate gland (P), the major pelvic tissue types were also segmented for thermal simulation. These included the rectal wall (RW), the peri-rectal fatty tissue (RF), the peri-prostatic fatty tissue (PF), the peri-prostatic venous plexus (PV), and the urinary bladder (B) (Fig. 1). These tissues were within the boundaries of anterior lower abdominal wall, bilateral pelvic walls, and sacrum. The manual segmentation was done using both NFS-T2WI and FS-T2WI prostate MR images, performed by an experienced radiologist (JHC) with 20 years of experience in interpreting body MRI. Since each pelvic tissue type normally covered several slices, a slice thickness of 4 mm through the middle of the prostate would contain these tissues unless the amount was negligible in the entire pelvic region. Muscles in the pelvic wall, the anterior lower abdominal wall, and the gluteal area did not directly contact with the rectum or the prostate gland and therefore not included in the analysis. The peri-rectal fat, the peri-prostatic fat, the cooling balloon and the urinary bladder were segmented on NFS-T2WI, while the prostate, the rectal wall and the peri-prostatic venous plexus were segmented on FS-T2WI. The segmentation of the cooling balloon was based on the location of the endorectal MR coil. The NVB was located in the posterior-lateral margin of the prostate gland, but it could not be seen on either NFS-T2WI or FS-T2WI due to its similar signal intensity with the peripheral zone of the prostate and the peri-prostatic venous plexus. However, since its anatomic location was well predictable, a small region of interest (ROI) for NVB was drawn at this location, shown in Fig. 1, for computing the temperature in the NVB.

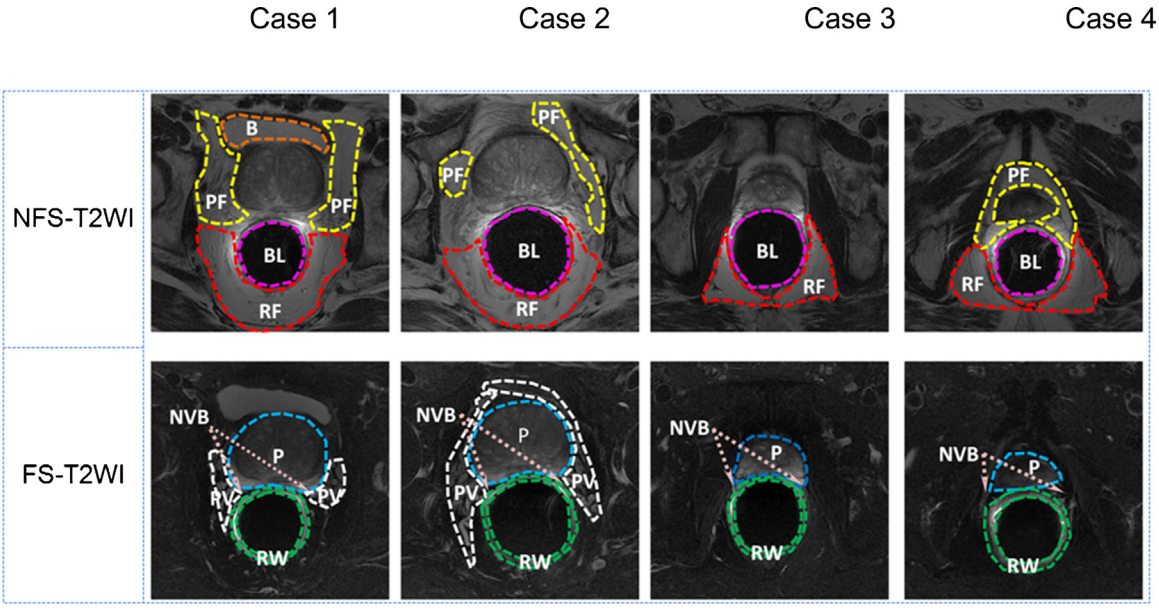

Fig. 1 – Segmentation of different tissue types. In NFS-T2WI (upper panel), *Purple*: endorectal cooling balloon (BL), *Yellow*: peri-prostatic fat (PF), *Red*: peri-rectal fat (RF), and *Orange*: urinary bladder (B). In FS-T2WI (lower panel), *Blue*: prostate gland (P), *Green*: rectal wall (RW) and *White*: peri-prostatic venous plexus (PV). The neurovascular bundle (NVB), which is located in the posterior-lateral margin of the prostate gland, is indicated by arrows on FS-T2WI. When there is an overlapping between peri-prostatic fat and peri-prostatic venous plexus, it is considered as peri-prostatic venous plexus. The pixel size is 0.39 mm × 0.39 mm, with an area of 0.15 mm^2. (For interpretation of the references to color in this figure legend, the reader is referred to the web version of this article.)

Table 1 – The area of the three major tissue components measured on the selected 2D image slice for simulation.

	Prostate size (cm^2)	Peri-prostatic + peri-rectal fat (cm^2)	Peri-prostatic venous plexus (cm^2)
Case 1	23.2	37.4	7.6
Case 2	22.6	26.7	16.4
Case 3	7.4	14.7	Not visible
Case 4	4.6	26.6	Not visible

The four cases analyzed in this study have different pelvic tissue compositions. A summary of the tissue volume for each case is given in Table 1. The area of each segmented tissue on the analyzed image is calculated by the number of pixels multiplied by the pixel size of 0.15 mm^2. Case #1 and Case #2 have relatively large prostate and abundant peri-prostatic venous plexus. In contrast, Case #3 and Case #4 have small prostate and negligible amount of peri-prostatic venous plexus. For these 2 cases, the peri-prostatic venous plexus is not visible on the selected slice, also not visible on four adjacent slices in both superior and inferior directions.

2.3. *Temperature simulation using bioheat transfer models*

The Pennes' bioheat thermal model is used to describe the temperature distribution dynamics [19,26]

$$\rho c \frac{\partial T(\vec{r}, t)}{\partial t} = \nabla(k\nabla \cdot T(\vec{r}, t)) + Q - c_b\omega_b(T(\vec{r}, t) - T_a) \quad (1)$$

where density (g/mm^3), specific heat (J/(g °C)) and thermal conductivity (W/(mm °C)) of the biological tissue are represented by ρ, c and κ. T is the temperature of the medium (°C), which is a function of time and space. The second term on the right hand side of Eq. (1) is the external power input deposition, which is neglected in this study due to the lack of external energy source such as focused ultrasound or laser irradiation. The last term on the right side of the equation represents the blood perfusion (heat sink) term where, ω_b is the blood perfusion rate (g/(mm^3 s)), c_b is the blood specific heat (J/(g °C)) and T_a is the supplying blood temperature (°C).

Finite element model (FEM) has been used to solve bioheat transfer equation for various applications such as high-intensity focused ultrasound (HIFU), conformal transurethral ultrasound therapy and laser ablation [27]. In this study, a FEM based solver is developed for modeling ECB cooling at pelvic region. To simplify the formation of the weak form of the heat transfer equation, we assume the blood flow temperature (T_a) and surrounding tissue temperature (T_f) to be body temperature 37 °C. Let

$$T' = T - 37\ ^\circ C \quad (2)$$

The weak form then can be expressed as:

$$\sum_n \int_\Omega d\vec{x}(\rho c \cdot \varphi\Phi_x)\frac{dU_n(t)}{dt} + \sum_n \left[\int_\Omega d\vec{x}\nabla\varphi \cdot (\kappa\nabla\Phi_x) + \int_\Omega d\vec{x}c_b\omega_b\varphi\Phi_x + \int_{\partial\Omega} d\vec{s}h\varphi\Phi_x\right]U_n(t) = 0 \quad (3)$$

where the solution of temperature is expanded in FEM basis as: $T(r, t) = \sum_n U_n(t)\Phi_x$. The test function, φ, is chosen to be piecewise linear function. The initial condition is set at 37 °C body temperature homogeneously. Due to the use of patient-specific anatomic model, the boundary condition for heat transfer is very complex. In this study, we consider only heat convection at the boundary, which is:

$$-k\frac{\partial T(r)}{\partial n} = h(T(r) - T_f) \quad (4)$$

where h is the heat transfer coefficient (W/(mm^2 °C)), between the surface of the medium and the surrounding medium at temperature T_f (°C). The simulation time step was chosen to be 5 s. We have tested different time steps, and found that when 5 s were used, the change of temperature between two time points was smaller than 1%, and we could precisely determine the temperature-time course.

The MRI segmentation and finite element mesh-based numerical solver were done using in-house programs written in MATLAB, and the analysis was carried out on a customized core 2 duo 3.0 GHz single-board computer equipped with 8 Gigabytes of memory. The MRI images were uploaded in MATLAB and the segmentation for each tissue type was done using manual drawing. The image domain was then discretized into a homogeneous triangle mesh with 8321 nodes and 16,384 elements using MATLAB built-in partial differential equation toolbox, and the mesh resolution was approximately 2 mm, which was considerably smaller compared to the organ size. The time step was discretized using implicit method, and thus with unconditional stability. The result from finite element solver was extrapolated back to the 512 × 512 image space, and the temperature for each pixel was obtained. The mean temperature in each analyzed ROI was calculated by averaging over all pixels contained within the ROI.

2.4. *Patient specific 2D simulation studies*

The 2D simulation for one case took about 1.5 h to complete. The thermal property of each tissue type is listed in Table 2. The thermal properties of rectal wall and prostate were considered the same as that of muscle, as the values were very similar in the literature [28–30]. The peri-rectal fat and peri-prostatic fat were assigned to the same value [30], as they were the same fat tissues at different anatomic locations. The cooling balloon and bladder were also considered to have the same thermal property as that of pure water. Lastly, the remaining un-segmented tissue was considered as homogeneous tissue with thermal property the same as that of muscle. The peri-prostatic venous plexus was regarded as slow flowing blood, and the blood perfusion rate was $\omega_b c_b = 16.0 \times 10^{-6}$ J/(mm^3 s °C) [31–34]. The blood perfusion

Table 2 – The thermal property of each segmented tissue type.

Tissue	Thermal conductivity ($\times 10^{-3}$ W/(mm °C))	Density · Heat capacity ($\times 10^{-3}$ J/(mm^3 °C))	References
ECB	0.58	4.2	[30]
Bladder	0.58	4.2	[30,35]
Fat	0.2	2.0	[30,35]
Prostate	0.5	3.6	[36–38]
Rectal wall	0.5	3.6	[30,34,39,40]
Muscle	0.5	3.6	[41,42]
Peri-prostatic venous plexus	0.5	3.84	[41,42]

rates in all other tissues were considered the same as that of resting muscle $\omega_b c_b = 0.6 \times 10^{-6}$ J/(mm^3 s °C) [26,33–35]. The value of thermal property for different tissue types varied, but it was not possible to measure them for each subject so we chose to use a reasonable estimation. In order to investigate the impact of different parameters, we have used different values for prostate thermal conductivity and venous blood flow rates in the temperate mapping.

The use of local hypothermia should confer no additional risk to the patient, when set above the limits of what has been safely reported (4 °C) for human use [31,43], even though cold saline below 4 °C had been used on patients previously [18,19]. In our study, the cooling balloon temperature was set at 4 °C. The temperature distribution was calculated every 5 s, for a total duration of 3 h. The temperature maps acquired at 0.5, 1, 2 and 3 h after the initiation of cooling were obtained. At each time point, the reached temperature for the prostate and the NVB was calculated by averaging the simulated temperatures over the ROI. To demonstrate the cooling effect propagating through the prostate, the temperature at anterior boarder and posterior boarder for each time points were also presented. As the posterior prostate was the closest to the cooling balloon, and the anterior prostate was the farthest, their temperature results showed the range within the prostate.

2.5. *Three-dimensional (3D) volumetric simulation*

Lastly, in one case we constructed a 3D volumetric model using all segmented tissues from multiple slices for simulation, so the obtained results could be compared to those of 2D model. Briefly, the different tissue types as considered in the 2D model were segmented from all acquired imaging slices, and they were stacked together using the thickness of 4 mm. The boundaries between the adjacent slices were smoothed using interpolation. The construction of 3D FEM formulation was following the same method described in Section 2.3. Tetrahedral mesh in a volume of 200 mm × 200 mm × 88 mm was constructed. The in-plane resolution on each transverse slice was reduced to 128 × 128 pixels to accommodate the large difference between the in-plane spatial resolution (0.4 mm for 512 pixel resolution) and the slice thickness (4 mm). A total of 565,633 tetrahedral elements were generated for 3D modeling, and the computational time for a 3D model took about 72 h to complete.

3. Results

The results from all 4 cases are shown in Fig. 2. The temperature distribution maps at four time points (0.5, 1, 2 and 3 h after cooling is started) are overlaid on the NFS-T2W MR images. The temperature scale is fixed from 15 to 35 °C. Cases #1 and #2 had more abundant peri-prostatic venous plexus compared to Cases #3 and #4. The results showed that Cases #3 and #4 could be cooled down much faster. The NVB for Cases #3 and #4 could be cooled down below 25 °C very quickly within the first 30 min. At 30 min time point, the averaged temperature in the whole prostate was 22.9 °C for Case #3, and 26.5 °C for Case #4. Cases #1 and #2 had large prostate sizes, with 7.6 cm^2 and 16.4 cm^2 peri-prostatic venous plexus, and the averaged temperature in the prostate and NVB could not reach 25 °C at the end of 3 h of cooling.

3.1. *Effect of peri-prostatic venous plexus abundance*

To further isolate the effect of blood vessel "heat sink", the simulation for Cases #1 and #2 was carried out by setting the blood perfusion rate of peri-prostatic venous plexus the same as that of muscle. The temperature distribution with/without the heat sink effect for Case #2 is illustrated in Fig. 3, and the results are summarized in Table 3. In the absence of vascular "heat sink", the NVB reached 26.1 °C after half an hour, and 22.1 °C after 3 h. The whole prostate reached near 25 °C after 3 h. On the contrary, in the presence of blood supply, the NVB reached 29.8 °C after half an hour, and only 29.2 °C at 3 h; the whole prostate could only be cooled down to 28.8 °C at 3 h. Therefore, the presence of venous plexus made a large impact, reducing the cooling effect by approximately 12% in the prostate and 24% at NVB at 3 h. The posterior part of the prostate (14%) was affected about two times more than the anterior part (8%) at 3 h. Case #1 had a smaller amount of venous plexus (7.6 cm^2) than Case #2 (16.4 cm^2), and the impact of the venous plexus was smaller. The reduced cooling due to the presence of venous plexus was approximately 8% in the prostate and 15% in NVB for Case #1 at 3 h, which was much less compared to the 12% and 24% for Case #2.

3.2. *Effect of prostate size*

Cases #1 and #2 had larger prostate size compared to Cases #3 and #4. In the meantime, Cases #1 and #2 also had a higher amount of peri-prostatic venous plexus, and as such it was difficult to evaluate whether ECB cooling was affected by prostate size or blood vessel abundance. Therefore, we evaluated the prostate size effect in the *absence* of vascular "heat sink". As shown in Fig. 2, the temperature of the whole prostate reached 19.6 °C for Case #3 at 3 h, and 23.2 °C for Case #4. For Case #1 in the *absence* of vascular "heat sink", the whole prostate only

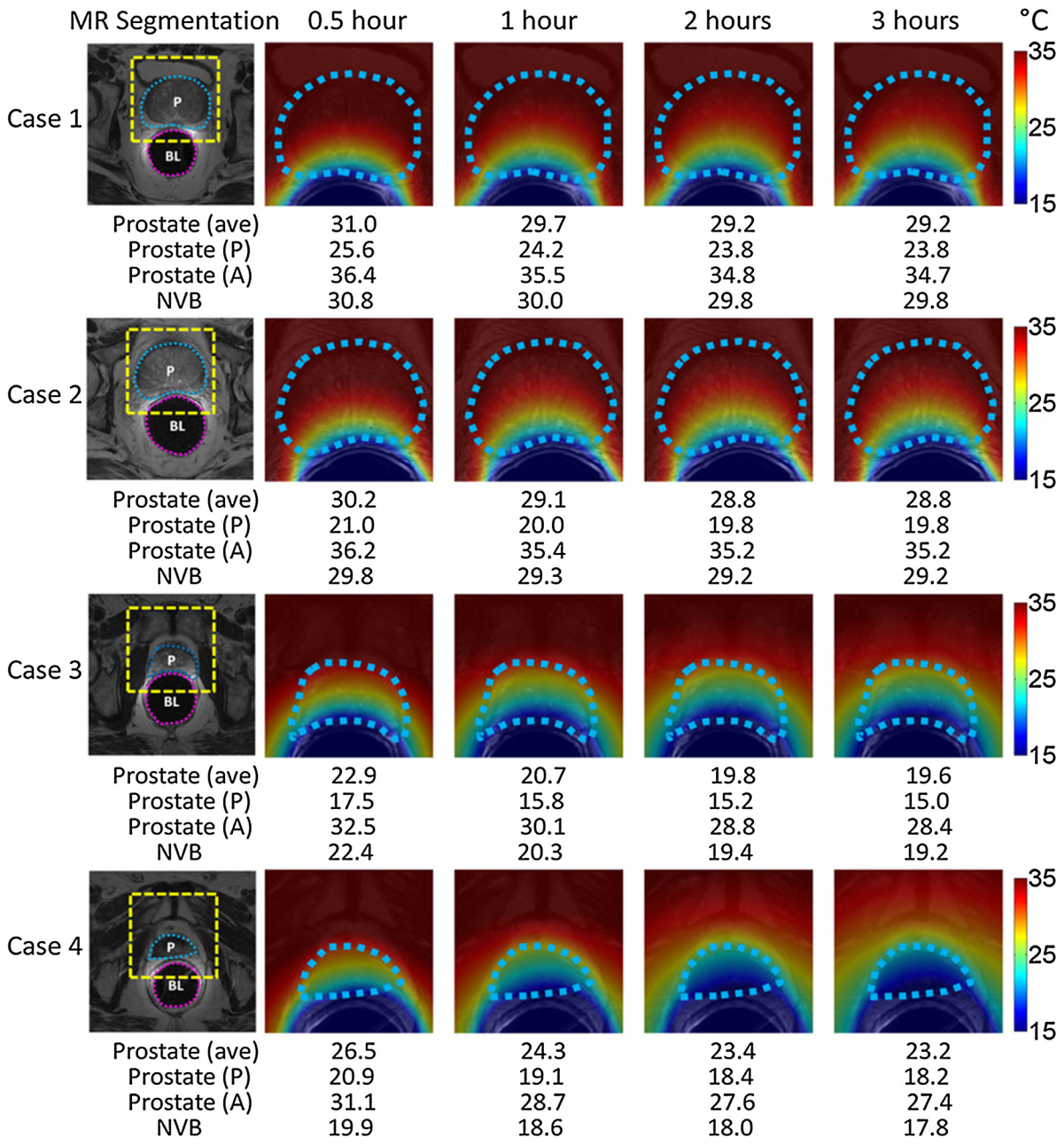

Fig. 2 – The segmented MR image is shown in the first column as the reference. The location of the balloon and prostate is indicated in purple and blue dashed lines. In columns 2–5, the temperature distribution in the yellow dashed box (magnified, the same size for all cases) is shown at four time points after the ECB cooling. The temperature distribution map is overlaid on the MR image, and the boundary of the prostate is shown in blue dashed lines. The averaged temperature from all pixels contained within the prostate gland (ave), the posterior boarder of the prostate (P), the anterior boarder of the prostate (A) and the temperature in the neurovascular bundle (NVB) ROI are shown for each case. The temperatures at the posterior and anterior boundaries indicate the range of temperature within the prostate. (For interpretation of the references to color in this figure legend, the reader is referred to the web version of this article.)

reached 27 °C at 3 h. Similarly, the whole prostate of Case #2 reached 25.3 °C at 3 h. The results showed that the larger the prostate was, the more difficult it was to cool down the whole prostate using ECB, even without the warming effect from surrounding vascular structure. Large prostate made the cooling difficult to propagate through the prostate. Even though the posterior part of the prostate was cooled quite effectively for Cases #1 and #2 (23.8 °C and 19.8 °C, respectively), the anterior part could not be cooled below 30 °C. In contrast, for Cases #3 and #4, the posterior prostate was very cold (15.0 °C and 18.2 °C) and the anterior part of prostate could be cooled down to 28.4 °C and 27.4 °C after 3 h.

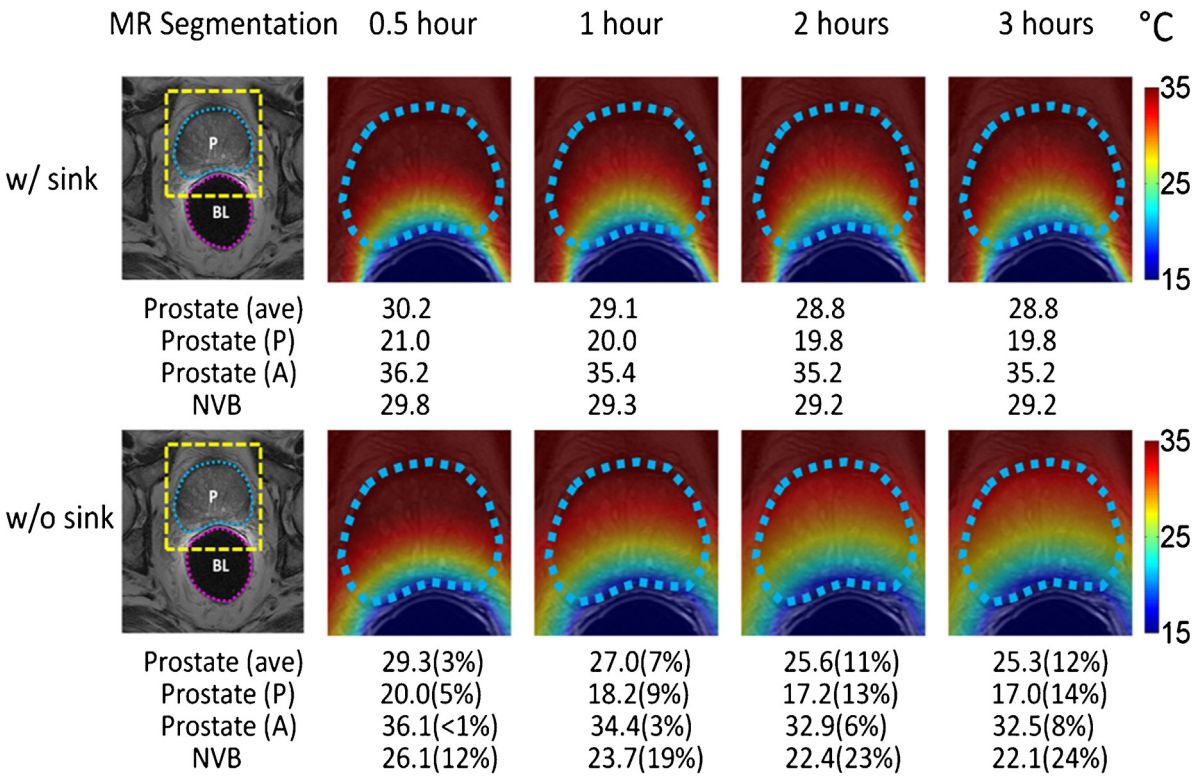

Fig. 3 – The results of heat sink effect. The simulation for Case #2 is carried out by setting the blood perfusion rate in the peri-prostatic venous plexus the same as that of muscle, to simulate the situation without the heat sink. The temperature distribution map is overlaid on the MR image, and the boundary of the prostate is shown in blue dashed lines. The averaged temperature from all pixels contained within the prostate gland (ave), the posterior boarder of the prostate (P), the anterior boarder of the prostate (A) and the temperature in the neurovascular bundle (NVB) ROI are shown. The temperature is lower without the heat sink, particularly noticeable in the NVB. (For interpretation of the references to color in this figure legend, the reader is referred to the web version of this article.)

Table 3 – The impact of venous plexus as the heat sink on the calculated temperature in the prostate and the NVB. All temperature is in unit of °C.

	0.5 h	1 h	2 h	3 h
Case #1 (7.6 cm^2)				
With heat sink				
Prostate (ave)	30.1	29.7	29.2	29.2
Prostate (A)	25.6	24.2	23.8	23.8
Prostate (P)	36.4	35.5	34.8	34.7
NVB	30.8	30.0	29.8	29.8
Without heat sink				
Prostate (ave)	30.5 (2%)	28.6 (4%)	27.4 (6%)	27.0 (8%)
Prostate (A)	25.3 (1%)	23.2 (4%)	22.1 (7%)	21.8 (8%)
Prostate (P)	36.4 (<1%)	35.2 (1%)	34.0 (2%)	33.6 (3%)
NVB	29.0 (6%)	26.7 (11%)	25.5 (14%)	25.2 (15%)
Case #2 (16.4 cm^2)				
With heat sink				
Prostate (ave)	30.2	29.1	28.8	28.8
Prostate (A)	21.0	20.0	19.8	19.8
Prostate (P)	36.2	35.4	35.2	35.2
NVB	29.8	29.3	29.2	29.2
Without heat sink				
Prostate (ave)	29.3 (3%)	27.0 (7%)	25.6 (11%)	25.3 (12%)
Prostate (A)	20.0 (5%)	18.2 (9%)	17.2 (13%)	17.0 (14%)
Prostate (P)	36.1 (<1%)	34.4 (3%)	32.9 (6%)	32.5 (8%)
NVB	26.1 (12%)	23.7 (19%)	22.4 (23%)	22.1 (24%)

The (percentage) shows the percent difference in cooling, simulated without compared to with heat sink. ave: average; A: anterior; P: posterior.

3.3. *Effect of fatty tissue*

Fatty tissue has shown to be less thermal conductive than other tissue types such as muscles [23], and thus can be considered as an insulating layer to block the cooling transfer or to protect the cooling loss. In this study, we evaluated how the peri-rectal and peri-prostatic fat affect ECB cooling. Case #4 had more fatty tissue volume than Case #3 (26.6 vs. 14.7 cm^2), especially prostatic fat. The temperature for the whole prostate reached below 20 °C after 2 h cooling for Case #3, but stayed above 20 °C for Case #4 even after 3 h. Case #4 had thicker rectal wall and fatty tissue layering between the rectal wall and the prostate, and these factors could hinder the cooling propagation, while the cooling balloon in Case #3 almost directly abutted the prostate, which allowed a closer contact and more efficient cooling.

To further investigate the impact of the fatty tissue effect, a simulation for Case #4 was carried out by setting the thermal property of fat to be the same as that of muscle. The results are summarized in Table 4. After half an hour, the NVB temperature with and without fatty tissue effect was 19.9 °C and 20.5 °C, respectively. The difference became less obvious after 3 h of cooling, 17.8 °C and 17.5 °C, respectively. Overall, the effect is small. A considerable amount of prostatic fat may retain the cooling, but only within 1 °C (and less than 5%) at all the time points for both NVB and whole prostate.

3.4. *Effect of tissue thermal property selection based on literature*

The literature value of thermal property for different tissue types varied, so we also investigated the effect of prostate thermal conductivity values and venous blood flow rates on the temperature mapping. Case #1 was used for this simulation. The prostate thermal conductivity was set to range from low (0.45×10^{-3} W/(mm °C)) [37] to high (0.56×10^{-3} W/(mm °C)) [41], and the results are shown in Table 5. The whole prostate temperature at the end of 3 h cooling differed about 1%, and the NVB region differed about 2%.

The venous blood perfusion rate ranged from slow (BPH patients: 10.8×10^{-6} J/(mm^3 s °C)) to fast (prostatic cancer patients: 29.0×10^{-6} J/(mm^3 s °C)) [33,34,44], and the results are shown in Table 6. The whole prostate temperature at the end of 3 h cooling differed about 2%, and the NVB region differed about 5%.

3.5. *Effect of enlarged bladder during cooling*

The effect of increased bladder size was also evaluated in this study. The test subject for this simulation was Case #1. The ECB cooling procedure may last for several hours. During this period, the intravenous (IV) infusion of fluid will cause the urine to accumulate in the bladder. In an imaging study using computed tomography, it was reported after 90–120 min of osmolar contrast injection the patient may express a desire to void [45]. With slower IV drips of isotonic saline, the filling of the bladder should be slower and therefore we assumed the bladder volume started to increase after 30 min and continued to increase by 100% at the end of 3 h [46]. All results for the whole prostate and the NVB region were not affected by the bladder expansion. At the end of 3 h, the difference of whole prostate temperature with bladder expansion (29.17 °C) and without (29.15 °C) was less than 0.1 °C, and the difference in NVB temperature was even less. As the bladder is far away from the prostate, the expansion containing more warm urine does not seem to affect the cooling.

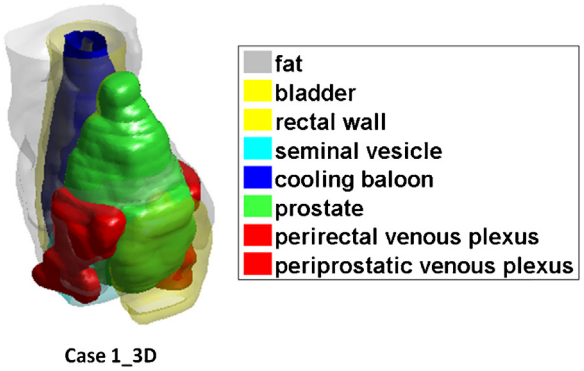

Fig. 4 – The reconstructed 3D volumetric model of Case #1 for 3D simulation. The prostate, cooling balloon and the venous plexus are shown with solid color, and other tissues are set to have high transparency for better visibility. (For interpretation of the references to color in this figure legend, the reader is referred to the web version of this article.)

3.6. *3D volumetric simulation*

The 3D simulation was carried out for Case #1 for comparison with the 2D simulation. The manual segmentation was done slice-by-slice and reconstructed into a 3D model, shown in Fig. 4. The 3D tetrahedral mesh was generated using MATLAB and the same heat transfer solver and thermal parameters were used for 3D simulation. The volumetric temperature distribution of the prostate at four times points (0.5, 1, 2 and 3 h) after the ECB cooling is shown in Fig. 5. The 100% (dark blue color) is defined as −12 °C change, which is correspondent to the cooling down to the 25 °C tissue temperature. The temperature change is only shown for the prostate gland for clarity. It can be seen that for the prostate tissue not adjacent to venous plexus, the cooling is more effective (faster and can reach a lower temperature). For each time point, cross-sectional temperature distributions at 5 locations are also shown.

The corresponding slice used in the 2D simulation is extracted from the 3D results for comparison. The temperature of the prostate and NVB is cooled down to 27.2 °C and 28.0 °C when the simulation is carried out in 3D, which is colder than the 29.2 °C and 29.8 °C obtained in 2D simulation. The difference is primarily due to the contribution of periprostatic venous plexus. The area of venous plexus measured from the slice used in 2D simulation is 7.6 cm^2, and the amount is lower in the adjacent superior (4.7 cm^2) and inferior (6.3 cm^2) slices. The reduced amount of venous plexus is considered in the 3D simulation, resulting in a lower temperature (better cooling).

Table 4 – The impact of fatty tissue on the calculated temperature in the prostate and the NVB of Case #4. All temperature is in unit of °C.

	0.5 h	1 h	2 h	3 h
With fatty tissue				
Prostate (ave)	26.5	24.3	23.4	23.2
NVB	19.9	18.6	18.0	17.8
Without fatty tissue				
Prostate (ave)	26.6 (<−1%)	24.3 (0%)	23.0 (2%)	22.7 (2%)
NVB	20.5 (−3%)	18.7 (−1%)	17.8 (1%)	17.5 (2%)

The (percentage) shows the percent difference in cooling, simulated without compared to with fatty tissue.

Table 5 – The impact of prostate thermal conductivity on the calculated temperature in the prostate and the NVB of Case #1. All temperature is in unit of °C.

	0.5 h	1 h	2 h	3 h
0.45×10^{-3} W/(mm °C)				
Prostate (ave)	31.1	29.9	29.4	29.3
NVB	31.0	30.2	30.0	30.0
0.56×10^{-3} W/(mm °C)				
Prostate (ave)	30.7 (1%)	29.5 (1%)	29.0 (1%)	29.0 (1%)
NVB	30.6 (1%)	29.8 (1%)	29.6 (1%)	29.5 (2%)

The (percentage) shows the percent difference in cooling, simulated with a higher compared to a lower prostate thermal conductivity.

Table 6 – The impact of venous blood perfusion rate on the calculated temperature in the prostate and the NVB of Case #1. All temperature is in unit of °C.

	0.5 h	1 h	2 h	3 h
10.8×10^{-6} J/(mm^3 s °C)				
Prostate (ave)	30.9	29.5	29.0	28.9
NVB	30.4	29.4	29.1	29.1
29.0×10^{-6} J/(mm^3 s °C)				
Prostate (ave)	31.1 (<1%)	30.0 (2%)	29.6 (2%)	29.5 (2%)
NVB	31.4 (3%)	30.8 (5%)	30.7 (5%)	30.6 (5%)

The (percentage) shows the percent difference in cooling, simulated with a higher compared to a lower venous plexus perfusion rate.

4. Discussion

We have shown that the hypothermic cooling using an endorectal balloon through the rectum wall across the urogenital pelvis can be simulated for each individual subject based on MR anatomical images. The prostate gland, the rectal wall and the tissues surrounding these two structures (mainly fat and venous plexus) are considered in the simulation. Four cases were analyzed in this study. For each case a 2D slice that has the largest cross-sectional area of the prostate gland was selected for 2D simulation. In one case, we have constructed a 3D model using segmented tissues from multiple slices, and performed the 3D volumetric simulation for comparison with 2D results.

Due to the limited patient data, there is no conclusive target temperature of ECB cooling from literature. However, it has been shown that the average intracorporeal temperature of ECB cooling for 112 patients was approximately 25 °C [18], thus it was used as the desired temperature in this study. In addition, there was no observed damage in the rectal wall caused by the cooling balloon. The local cooling did not induce any observable global body temperature change. The experience suggested that maintaining the balloon temperature at 4 °C is safe for patients.

As expected, the simulation results show that the cooling can vary substantially depending on the pelvic anatomy of each patient. Such simulation tool may serve as guidance for physicians to determine the optimal ECB experimental set-up for each individual patient before the surgery. For example, a patient with minimal venous plexus tissue may easily reach the desired 25 °C temperature 30 min after the cooling (like Cases #3 and #4). On contrary, patients like Cases #1 and #2 may have difficulty to be cooled down, and the modification of the ECB set-up (e.g., by expanding the volume of cooling balloon or lowering the temperature of circulating saline) is needed to reach the desired cooling temperature. It has been observed that during surgery the muscle and fat can be cooled more effectively than the NVB, because the nerve fibers in the NVBs are constantly supplied by warm blood supply [31]. The venous plexus will act as the “heat sink”, and diminish the cooling effect. For patients with abundant peri-prostatic venous plexus, their prostate and NVB region are expected to be more difficult to be cooled down. As shown in Table 3, for Case #2 the presence of venous plexus can reduce the cooling effect by 24% in the NVB at 3 h. Therefore, it is essential

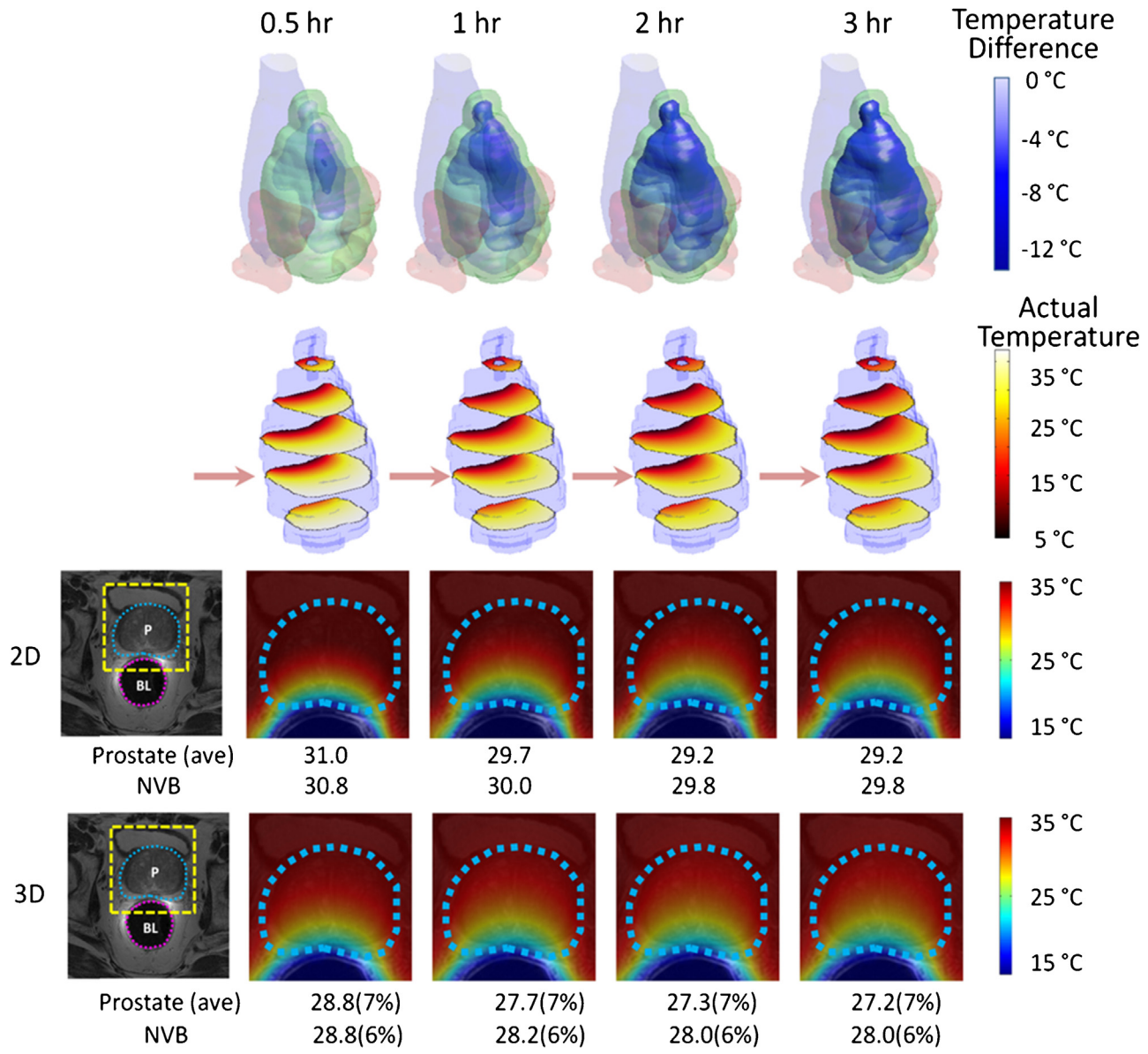

Fig. 5 – The 3D simulation results for Case #1. The volumetric temperature distribution in the prostate at four time points after ECB cooling is shown. On the first row, the prostate turns to dark blue (–12 °C) gradually, indicating that it has reached the desired temperature of 25 °C. The temperature maps at five cross-sectional slices are shown on the second row, demonstrating the propagation of cooling from posterior toward anterior of the prostate. The results of the corresponding slice used in 2D simulation are extracted from the 3D matrix for side-by-side comparison, using the same format as in Fig. 1. The averaged temperature from all pixels contained within the prostate gland (ave) and the temperature at the NVB ROI are shown. The results show that the temperature obtained in 3D simulation is lower, mainly because the reduced amount of venous plexus in adjacent slices is considered. The percent difference in the 3D compared to the 2D is shown in the parenthesis. (For interpretation of the references to color in this figure legend, the reader is referred to the web version of this article.)

to take the vascular structure into account for optimizing ECB nerve-sparing cooling and prostate cooling for each individual patient.

Another factor that can affect the cooling effect is the prostate size. In this simulation, we have shown that patient with a larger prostate was more difficult for the whole prostate to be cooled down. In contrast, the presence of fatty tissue only affected the cooling effect minimally, approximately by 1–2%, and thus can be ignored. Lastly, we showed that using different values of prostate thermal conductivity and blood perfusion rate reported in the literature only had 2–5% change in the temperature.

The anterior prostate region is less protected by the hypothermic effect, due to its relatively far distance from the ECB. Considering the potential complications of urine incontinence and sexual dysfunction related to radical

prostatectomy, this area is, however, less relevant. Because damage of anatomic structures potentially leading to urine incontinence and sexual impotence are mainly located in the posterior aspect (NVB) and inferior aspect (bladder neck and urethrae) of the prostate, which are near the ECB and can usually be cooled well.

The comparison of 2D and 3D simulation results show that the distribution of the venous plexus is the major factor to account for the differences in the simulated temperatures. As shown in Fig. 4, the highest amount of venous plexus is located around the base of prostate, corresponding with the largest cross-sectional area the prostate on the 2D transverse plane. Therefore, what we present in 2D is the "worse case scenario". Furthermore, the NVB on this plane is very close to the prostate and most likely to be affected by the surgical procedure. From a clinical application standpoint, the results analyzed using this 2D slice provide a conservative prediction. Therefore, although the 2D slice does not represent the entire 3D prostate, the obtained results from this 2D slice may provide important information for NVB protection.

Segmentation of various tissue types is performed manually in this study. Certainly performing automatic segmentation using computer programs is preferred, but as the first step we try to identify tissues that need to be considered in the simulation model. The complexity of the pelvic structure makes intensity based or mutual information based segmentation almost impossible. Atlas based auto-segmentation of the prostate gland has been developed, but the robustness has not been proven yet [47–49]. Our study requires the segmentation of not only the prostate gland, but also other organs such as rectum, venous plexus, fatty tissue, bladder and NVB, which can only be reliably contoured by an experienced radiologist. Particularly, the distributions of fat and venous plexus are different from person to person, and it is not possible to use template-based or machine learning segmentation. Despite that, there is definitely room for improvements. After more datasets are analyzed, they can be used for training purposes. As our results suggest that the prostate and venous plexus are the most important structures to be considered in the model, they may be segmented using a combined Atlas-based and intensity-based auto-segmentation, and the results can be verified and modified by a radiologist before simulation.

The results obtained from the simulation model agree with the expectation, yet still need to be further refined and verified using thermometry mapping experiments in human subjects. In order to obtain patient-specific temperature measurements, currently two approaches can be used. (1) Mechanical temperature measurement device using needle electrode or probe [19]. The temperature reading is obtained point by point rather than a spatial/temporal distribution map through the whole region of concern, thus not optimal for comparison with our simulation results. (2) MR thermometry. The MR thermometry allows real-time, non-invasive, temperature mapping [18,46]. It has been used successfully in monitoring laser induced interstitial thermotherapy (LIIT) and focused ultrasound ablation [50,51]. This method can provide detailed spatial/temporal distribution of temperature of the prostate for verification of our simulation results. However, the most common method using proton resonance frequency (PRF) shift does not work in fatty tissues, and it is not able to provide the temperature mapping in the entire pelvic region, only the temperature for not-fat tissues. Nonetheless, it is sufficient for our study to measure temperatures in the prostate and NVB. After the simulation model is verified in human subjects using MR thermometry, it may provide a reliable guidance for the ECB cooling set-up before prostatectomy surgery.

As the first step in this proof-of-principle study, in the present work the simulation was done on a 2D slice. With a labor-intense manual segmentation effort and a much longer computation time, the method can be easily extended to 3D. One main purpose of this simulation is to evaluate the impact of several factors, including the volumes of venous plexus, prostate, fat, as well as the thermal property parameters used in the simulation; therefore, using a simplified 2D slice (and even controlling for some parameters) can give us a clear understanding about their respective impacts on the cooling effect. After we have gained a substantial knowledge about the simulation model and shown that it can yield reasonable results, the next step is to analyze a larger dataset from more patients using a 3D model to systematically investigate the impact of multiple factors together and study how they interfere with each other. The ultimate goal of this project is to develop and validate a hypothermia surgical planning tool, similar to the development of automatic treatment-planning tools commonly used for radiation therapy. The key steps include: (1) perform an anatomic MR scan, (2) perform automatic segmentation, (3) perform bioheat simulation, (4) display temperature maps that can be achieved with the standard ECB set-up, and (5) based on results suggest modification of experimental set-up to reach desired temperature.

5. Conclusion

In conclusion, we have developed a computational model based on structures segmented on MR images to simulate the hypothermic cooling across the urogenital pelvis by inserting a cooling balloon into the rectum. The size of prostate (or, the distance of tissue from the cooling balloon) is a major factor determining the effect. For a patient with a considerable amount of vascular structure in pelvic region, it is difficult to cool down the NVB region and the whole prostate effectively. The prostate MR images may provide the individual anatomy and tissue components for such thermal modeling to be used in patient-specific treatment planning to achieve optimized cooling effect using ECB. In this study the simulation is done using a 2D model to demonstrate feasibility, and it is needed to expand to a more realistic 3D model and validated using thermometry results for future patient applications.

Conflict of interest

The authors have no conflict of interest to disclose.

Acknowledgements

This research is supported in part by the National Institutes of Health (NIH) grants R01EB008716, R01CA127927 and Susan G. Komen for the Cure post-doc training grant KG101442.

REFERENCES

[1] F.J. Fowler Jr., M.J. Barry, G. Lu-Yao, J. Wasson, A. Roman, J. Wennberg, Effect of radical prostatectomy for prostate cancer on patient quality of life: results from a medicare survey, Urology 45 (1995) 1007–1015.

[2] R. Kirschner-Hermanns, G. Jakse, Quality of life following radical prostatectomy, Crit. Rev. Oncol. Hematol. 43 (2002) 141–151.

[3] G.Y. Tan, S. Grover, A. Takenaka, P. Sooriakumaran, A.K. Tewari, Current concepts in cavernosal neural anatomy and imaging and their implications for nerve-sparing radical prostatectomy, in: A.K. Hemal, et al. (Eds.), Robotics in Genitourinary Surgery, Springer, London, 2011, pp. 273–289.

[4] G.Y. Tan, P.J. Dorsey, A.K. Tewari, Methods and maneuvers for improving functional outcomes during robotic radical prostatectomy complications of laparoscopic and robotic urologic surgery, in: R. Ghavamian (Ed.), Robotics in Genitourinary Surgery, Springer, New York, 2010, pp. 211–231.

[5] N. Ni Choileain, H.P. Redmond, The immunological consequences of injury, The Surgeon 4 (2006) 23–31.

[6] L. Osborn, Leukocyte adhesion to endothelium in inflammation, Cell 62 (1990) 3–6.

[7] S. Roujol, M. Ries, B. Quesson, C. Moonen, B. Denis de Senneville, Real-time MR-thermometry and dosimetry for interventional guidance on abdominal organs, Magn. Reson. Med. 63 (2010) 1080–1087.

[8] B. de Senneville, C. Mougenot, B. Quesson, I. Dragonu, N. Grenier, C. Moonen, MR thermometry for monitoring tumor ablation, Eur. Radiol. 17 (2007) 2401–2410.

[9] A.B. Holbrook, J.M. Santos, E. Kaye, V. Rieke, K.B. Pauly, Real-time MR thermometry for monitoring HIFU ablations of the liver, Magn. Reson. Med. 63 (2010) 365–373.

[10] T. Vogl, T. Lehnert, K. Eichler, D. Proschek, J. Flöter, M. Mack, Adrenal metastases: CT-guided and MR-thermometry-controlled laser-induced interstitial thermotherapy, Eur. Radiol. 17 (2007) 2020–2027.

[11] K.D. Schaser, A.C. Disch, J.F. Stover, A. Lauffer, H.J. Bail, T. Mittlmeier, Prolonged superficial local cryotherapy attenuates microcirculatory impairment, regional inflammation, and muscle necrosis after closed soft tissue injury in rats, Am. J. Sports Med. 35 (2007) 93–102.

[12] C.H. Yeh, Y.C. Wang, Y.C. Wu, Y.M. Lin, P.J. Lin, Ischemic preconditioning or heat shock pretreatment ameliorates neuronal apoptosis following hypothermic circulatory arrest, J. Thorac. Cardiovasc. Surg. 128 (2004) 203–210.

[13] T. McManus, M. Sadgrove, A.K. Pringle, J.E. Chad, L.E. Sundstrom, Intraischaemic hypothermia reduces free radical production and protects against ischaemic insults in cultured hippocampal slices, J. Neurochem. 91 (2004) 327–336.

[14] N. Kawamura, J.D. Schmelzer, Y. Wang, A.M. Schmeichel, P.A. Low, The therapeutic window of hypothermic neuroprotection in experimental ischemic neuropathy: protection in ischemic phase and potential deterioration in later reperfusion phase, Exp. Neurol. 195 (2005) 305–312.

[15] S. Westermann, B. Vollmar, H. Thorlacius, M.D. Menger, Surface cooling inhibits tumor necrosis factor-α-induced microvascular perfusion failure, leukocyte adhesion, and apoptosis in the striated muscle, Surgery 126 (1999) 881–889.

[16] C. Bleakley, S. McDonough, D. MacAuley, The use of ice in the treatment of acute soft-tissue injury, Am. J. Sports Med. 32 (2004) 251–261.

[17] D.S. Finley, A.J. Costello, T.E. Ahlering, Cautery-free technique of robot-assisted radical prostatectomy: impact on nerve preservation and long-term outcome on recovery of sexual function robotics in genitourinary surgery, in: A.K. Hemal, et al. (Eds.), Robotics in Genitourinary Surgery, Springer, London, 2011, pp. 261–272.

[18] D.S. Finley, K. Osann, A. Chang, R. Santos, D. Skarecky, T.E. Ahlering, Hypothermic robotic radical prostatectomy: impact on continence, J. Endourol. 23 (2009) 1443–1450.

[19] D.S. Finley, A. Chang, B. Morales, K. Osann, D. Skarecky, T. Ahlering, Impact of regional hypothermia on urinary continence and potency after robot-assisted radical prostatectomy, J. Endourol. 24 (2010) 1111–1116.

[20] D.S. Finley, E. Rodriguez Jr., D.W. Skarecky, T.E. Ahlering, Quantitative and qualitative analysis of the recovery of potency after radical prostatectomy: effect of unilateral vs bilateral nerve sparing, BJU Int. 104 (2009) 1484–1489.

[21] D.S. Finley, K. Osann, D. Skarecky, T.E. Ahlering, Hypothermic nerve-sparing radical prostatectomy: rationale, feasibility, and effect on early continence, Urology 73 (2009) 691–696.

[22] D.L. Pick, K. Osann, D. Skarecky, N. Narula, D.S. Finley, T.E. Ahlering, The impact of cavernosal nerve preservation on continence after robotic radical prostatectomy, BJU Int. 108 (2011) 1492–1496.

[23] K.C. Zorn, N. Bhojani, G. Gautam, S. Shikanov, O.N. Gofrit, G. Jayram, M.H. Katz, I. Cagiannos, L. Budaus, F. Abdollah, M. Sun, P.I. Karakiewicz, A.L. Shalhav, H.A. Al-Ahmadie, Application of ice cold irrigation during vascular pedicle control of robot-assisted radical prostatectomy: EnSeal instrument cooling to reduce collateral thermal tissue damage, J. Endourol. 24 (2010) 1991–1996.

[24] E.H. Kim, G.L. Andriole, Prostate-specific antigen-based screening: controversy and guidelines, BMC Med. 13 (2015) 61.

[25] S.A. Mirowitz, J.P. Heiken, J.J. Brown, Evaluation of fat saturation technique for T2-weighted endorectal coil MRI of the prostate, Magn. Reson. Imaging 12 (1994) 743–747.

[26] H.H. Pennes, Analysis of tissue and arterial blood temperatures in the resting human forearm, J. Appl. Physiol. 85 (1998) 5–34.

[27] E.H. Wissler, Pennes' 1948 paper revisited, J. Appl. Physiol. 85 (1998) 35–41.

[28] M.F. Marqa, P. Colin, P. Nevoux, S. Mordon, N. Betrouni, Focal laser ablation of prostate cancer: numerical simulation of temperature and damage distribution, Biomed. Eng. Online 10 (2011) 45.

[29] B. Mathieu, N.D. William Apoutou, K. Ilya, B. Michael, C. Rajiv, 3D conformal MRI-controlled transurethral ultrasound prostate therapy: validation of numerical simulations and demonstration in tissue-mimicking gel phantoms, Phys. Med. Biol. 55 (2010) 6817.

[30] M. Burtnyk, R. Chopra, M.J. Bronskill, Quantitative analysis of 3-D conformal MRI-guided transurethral ultrasound therapy of the prostate: theoretical simulations, Int. J. Hyperthermia 25 (2009) 116–131.

[31] F.A. Duck, Physical Properties of Tissue: A Comprehensive Reference Book, Academic Press, London, San Diego, 1990.

[32] Z.S. Deng, J. Liu, Blood perfusion-based model for characterizing the temperature fluctuation in living tissues, Physica A: Stat. Mech. Appl. 300 (2001) 521–530.

[33] H. Toma, R. Nakamura, S. Onitsuka, N. Goya, H. Nakazawa, Effect of endocrine treatment on prostatic blood flow in patients with prostatic adenocarcinoma, J. Urol. 140 (1988) 91–95.

[34] T. Inaba, Quantitative measurements of prostatic blood flow and blood volume by positron emission tomography, J. Urol. 148 (1992) 1457–1460.

[35] J.H. Wootton, A.B. Ross, C.J. Diederich, Prostate thermal therapy with high intensity transurethral ultrasound: the impact of pelvic bone heating on treatment delivery, Int. J. Hyperthermia 23 (2007) 609–622.

[36] V.J. Castelli, E.M. Stanley, Thermal conductivity of distilled water as function of pressure and temperature, J. Chem. Eng. Data 19 (1974) 8–11.
[37] H.S. Hatfield, L.G.C. Pugh, Thermal conductivity of human fat and muscle, Nature 168 (1951) 918–919.
[38] M.J. Morley, Thermal conductivities of muscles, fats and bones, Int. J. Food Sci. Technol. 1 (1966) 303–311.
[39] H.F. Bowman, E.G. Cravalho, M. Woods, Theory, measurement, and application of thermal properties of biomaterials, Annu. Rev. Biophys. Bioeng. 4 (1975) 43–80.
[40] J.C. Bischof, D. Smith, P.V. Pazhayannur, C. Manivel, J. Hulbert, K.P. Roberts, Cryosurgery of dunning AT-1 rat prostate tumor: thermal, biophysical, and viability response at the cellular and tissue level, Cryobiology 34 (1997) 42–69.
[41] M. Jankun, T.J. Kelly, A. Zaim, K. Young, R.W. Keck, S.H. Selman, J. Jankun, Computer model for cryosurgery of the prostate, Comput. Aided Surg. 4 (1999) 193–199.
[42] J.W. Valvano, J.T. Allen, H.F. Bowman, The simultaneous measurement of thermal conductivity, thermal diffusivity, and perfusion in small volumes of tissue, J. Biomech. Eng. 106 (1984) 192–197.
[43] T.A. Balasubramaniam, H.F. Bowman, Thermal conductivity and thermal diffusivity of biomaterials: a simultaneous measurement technique, J. Biomech. Eng. 99 (1977) 148–154.
[44] C.J. Diederich, E.C. Burdette, Transurethral ultrasound array for prostate thermal therapy: initial studies, IEEE Trans. Ultrason. Ferroelectr. Freq. Control 43 (1996) 1011–1022.
[45] J.K. Kim, J.H. Ahn, T. Park, H.J. Ahn, C.S. Kim, K.S. Cho, Virtual cystoscopy of the contrast material-filled bladder in patients with gross hematuria, Am. J. Roentgenol. 179 (2002) 763–768.
[46] A. Mandhani, J.P.J. Dorsey, R. Ramanathan, et al., Real time monitoring of temperature changes in neurovascular bundles during robotic radical prostatectomy: thermal map for nerve-sparing radical prostatectomy, J. Endourol. 22 (2008) 2313–2318.
[47] W. Li, A. Vassil, Y. Zhong, P. Xia, Daily dose monitoring with atlas-based auto-segmentation on diagnostic quality CT for prostate cancer, Med. Phys. 40 (2013) 1117–1120.
[48] J. Hwee, A.V. Louie, S. Gaede, G. Bauman, D. D'Souza, T. Sexton, M. Lock, B. Ahmad, G. Rodrigues, Technology assessment of automated atlas based segmentation in prostate bed contouring, Radiat. Oncol. 6 (2011) 110.
[49] K.S. Chao, S. Bhide, H. Chen, J. Asper, S. Bush, G. Franklin, V. Kavadi, V. Liengswangwong, W. Gordon, A. Raben, J. Strasser, C. Koprowski, S. Frank, G. Chronowski, A. Ahamad, R. Malyapa, L. Zhang, L. Dong, Reduce in variation and improve efficiency of target volume delineation by a computer-assisted system using a deformable image registration approach, Int. J. Radiat. Oncol. Biol. Phys. 68 (2007) 1512–1521.
[50] A. Kickhefel, J. Roland, C. Weiss, F. Schick, Accuracy of real-time MR temperature mapping in the brain: a comparison of fast sequences, Phys. Med. 26 (2010) 192–201.
[51] V. Rieke, K. Butts Pauly, MR thermometry, J. Magn. Reson. Imaging 27 (2008) 376–390.